Journal Pre-proof

Robust and conductive mesoporous reduced graphene oxide- silica hybrids achieved by printing and the sol gel route

J.J. Moyano, J. Loizillon, D. Pérez-Coll, M. Belmonte, P. Miranzo, D. Grosso, M.I. Osendi

PII: S0955-2219(20)30797-4

DOI: https://doi.org/10.1016/j.jeurceramsoc.2020.09.070

Reference: JECS 13624

To appear in: *Journal of the European Ceramic Society*

Received Date: 15 July 2020

Accepted Date: 30 September 2020

Please cite this article as: Moyano JJ, Loizillon J, Pérez-Coll D, Belmonte M, Miranzo P, Grosso D, Osendi MI, Robust and conductive mesoporous reduced graphene oxide- silica hybrids achieved by printing and the sol gel route, *Journal of the European Ceramic Society* (2020), doi: https://doi.org/10.1016/j.jeurceramsoc.2020.09.070

Robust and conductive mesoporous reduced graphene oxide- silica hybrids achieved by printing and the sol gel route

J.J. Moyano[1], J. Loizillon [2], D. Pérez-Coll[l], M. Belmonte[1], P. Miranzo[1], D. Grosso[2], M. I. Osendi[1*]

[1]Instituto de Cerámica y Vidrio, CSIC, Campus de Cantoblanco, 28049 Madrid, Spain

[2]Institut Materiaux Microélectronique et Nanosciences de Provence, Aix-Marseille Université, Faculté des Sciences de Saint Jérôme, 13397 Marseille Cedex 20, France

*Corresponding autor e-mail: miosendi@icv.csic.es (M. Isabel Osendi)

Graphical abstract

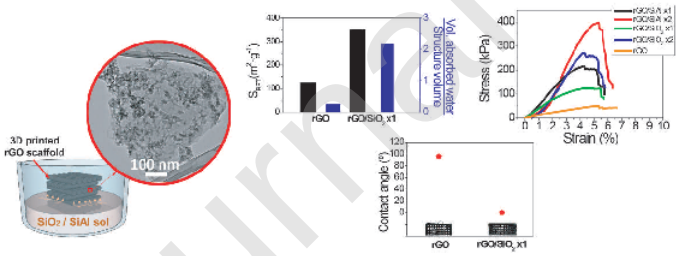

Abstract

Reduced graphene oxide (rGO) scaffoldings are used as templates to create lightweight 3D silica/rGO and silico-aluminate/rGO hybrids by a simple impregnation route and the sol-gel method. The printed rGO assemblies are infiltrated by the corresponding alkoxide precursor solution and gelled by exposition to ammonia vapours, producing hybrid replica of the rGO structure. The hybrids show a significant prevalence of mesopores, with total porosity above 94 %, density of ~ 0.1g·cm^{-3} and specific surface area ~2 times higher than the bare rGO structure. As results, the hybrid materials show enhanced water absorption capacity and hydrophilicity, display compressive strengths in the range 0.1 – 0.4 MPa, which scale with the proportion of silica (or Al-modified silica) on the bare rGO scaffold, and electrical conductivities are above 60 S·m^{-1}. These properties are very attractive for applications in the removal of pollutants, water filtering, catalysis, drug delivery, or energy production and storage.

Keywords: additive manufacturing; sol-gel; mesoporous silica; reduced, graphene oxide; lightweight materials

1. Introduction

Graphene has become a common element in research subjects connected with the energy production [1,2] and microelectronics [3,4], but also in the development of new technologies for example in the areas of biomedicine and sensing [5,6]. This material is normally used as thin layers and films [7] or as filler for the improvement of properties in all kinds of composites [8–11]. On the other hand, graphene and particularly graphene oxide (GO) are conceived as building blocks for making 3D connected lightweight structures of high porosity, normally maintaining high electric conductivity [12–15], flexibility and relatively high contact area [16–18]. These porous structures are often created via self-assembling routes, foam replication, chemically vapour deposition routes

or printing methods [12,13,15,16,19], and aimed for uses such as supercapacitors [20,21], catalysts [22,23], environmental remediation [24] or biomedical applications [25,26].

An alternative approach for extending the applications of these 3D graphene structures by addressing some of its shortcomings (i.e. weakness, air and flame exposure vulnerability, lack of porosity at different scales, etc) would entail making composites or hybrids by anchoring other species on the 3D graphene structure while maintaining the accessible porosity and cellular character [27–29]. In particular, our group has previously shown that via relatively simple methods, such as liquid infiltration with a preceramic polymer or via copper electrodeposition [30,31], it is possible to build complex composite and hybrid materials using printed GO scaffolds as templates/supports. Presently, we propose the infiltration of 3D printed reduced GO (rGO) structures with a well-known silica precursor, tetraethyl orthosilicate (TEOS) or alternatively, mixed with an Al_2O_3 precursor, and take advantage of the sol-gel route to build 3D silica/ silicoaluminate)/rGO hybrid materials that reproduce the 3D printed template.

Porous silica-graphene materials are attracting increasing attention due to the fine porosity generally induced when the sol-gel process is chosen. In some cases, the alkoxide solution is cast over the GO assembly [32.32] while a single step hydrothermal synthesis route is also reported [34]. Some of these SiO_2/rGO hybrid structures present high potential as oil absorbents [35], membranes for water filtration [36], nanocapsules for hoarding phase change materials aimed at thermal energy storage [37], or as superhydrophilic coating [38].

Silica aerogels are quite weak materials and difficult to shape once gelled [39]; accordingly, different efforts have been done for making a stronger silica backbone gel, including enhanced cross-linking between the aerogel particles with different polymers [39,40], and also adding a second phase in the form of particles or fibres. There are not

many studies reporting the effect of GO additions on the strength of silica aerogels [41,42], hence it seems attractive to look into possible synergetic effects between the GO and silica networks that may improve the mechanical integrity of the ensemble.

In this work, 3D silica/reduced GO hybrids are created by infiltration of rGO printed scaffolds making use of the sol-gel route, by means of a low temperature gel crosslinking with ammonia vapours. The method replicates the 3D printed structures but with a notable enhancement of the specific surface area and mesoporosity, while maintaining practically intact their electrical functionality and improving other characteristics of considerable practical interest like the strength, water absorption capacity or wettability of the structures.

2. Experimental

2.1 Preparation route for the composite scaffolds

Three-dimensional GO scaffold were printed by following a previously reported route [30]. In brief, a water-based ink was prepared with GO nanosheets (N002-PDE, Angstron Materials Inc.), nominally 2–3 nm thick and of length ≤ 7 μm, then an aqueous solution of two types of polyethylenimines (H-PEI, Mw=25,000 g mol^{-1}; L-PEI, Mw=2000 g mol^{-1} in a 50 wt. % aqueous concentration, both from Aldrich Chemical Co.) and polyethylene glycol (PEG, Mw=8000 g mol^{-1}, 60 wt.%; Fisher Scientific) were added and thoroughly stirred for complete homogenization in a high shear mixer (AR-250; Thinky Company). The typical ink composition is (all in wt. %) 4.8 GO, 7.2 H-PEI, 1.3 L-PEI, 3.6 PEG and 82.2 of added water (of controlled-conductivity σ=8 $M\Omega^{-1}$, pH=8.2). The ink filled printing syringe was housed in the three-axis robocasting system (A3200, 3-D Inks LLC) that executes printing controlled by 3D designer software (RoboCAD 4.2, 3-D Inks LLC). Cubic scaffolds (12.5 x 12.5 x 6.0, in mm) of 16 layers of evenly spaced

rods (780 μm gap) that were 90° turned relative to the adjacent layers were produced with a printing needle of 410 μm of diameter on alumina flat substrates.

The printed GO structures were frozen at once by plunging them into liquid nitrogen for 10 seconds, and then lyophilized (Freezone Plus 12L, Labconco Corp.), and then treated at 1200 ºC, in a graphitic furnace (HPW 150/200-2200-100AS, KCE), under nitrogen atmosphere (at 10 kPa) to burn out the organics in the ink and enhance GO reduction by removal of some oxygenated groups [13,30]. At this stage, the 3D rGO samples exhibited on average dimensions 12.0 x 12.0 x 5.0, in mm.

A solution containing tetraethyl orthosilicate (TEOS, 98% from Aldrich Chemical Co.), ethanol (EtOH), deionized water and hydrochloric acid (HCl, 1M), in the proportions given in Table 1, was prepared and magnetically stirred at 70 °C until becoming clear (~5 min), named SiO_2 sol. Equal procedure was followed for preparing the second solution, labelled as SiAl sol; in this case, the mixture was completed with certain amount (see Table 1) of aluminium chloride ($AlCl_3$ Msynth@plus, Merck Group).

Table 1. Composition (in molar ratio) of the prepared Si and SiAl sols

	TEOS	**$AlCl_3$**	**H_2O**	**HCl (1M)**	**EtOH**
SiO_2	1	-	3	2	10
SiAl	0.9	0.1	3	2	10

The rGO scaffolds were half immersed in each sol and maintained for 5 minutes within an airtight container. The impregnated scaffolds, after removal of the liquid excess with absorbent paper, were placed in a container with a solution of $NH_3 \cdot H_2O$ (1:3), on a platform resting ~5 mm above the liquid level to avoid direct contact with the basic solution. Samples were hold for 24 hours at room temperature in this sealed container to

induce extended condensation and rigidness of the impregnated intermediate xerogel through ammonia catalysis (*e.i.* Ammonia Vapour Treatment (AVT) [43]). Afterwards, the scaffolds were washed in EtOH to remove any vapour condensation residues. A schematic description of the entire process is displayed in Fig.1. A set of rGO samples was subjected to the same (infiltration and gelling) procedure twice, for each sol (samples labelled as "x2"). Alternatively, few of the just infiltrated scaffolds for both sols were treated at 200 ºC (15 minutes) under a flowing nitrogen atmosphere (1 bar) to reveal the effect of the thermal curing as compared to the AVT.

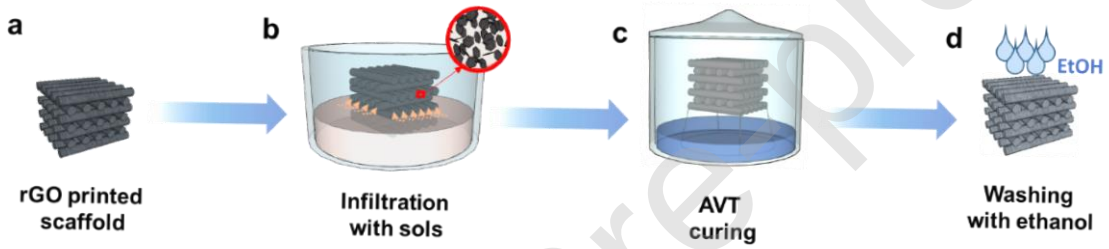

Fig 1. Schematic of the synthesis process used for fabricating silica (or SiAl)-rGO hybrids via infiltration of the 3D rGO scaffold (a,b), gelling with basic vapours (c) and ethanol washing (d).

2.2 Characterization and property measurement methods

The geometric density (ρ_{geo}) of each specimen was estimated by weighing the samples in a precision balance and measuring them with a digital calliper. The pore size distribution of the infiltrated skeletons was evaluated from the nitrogen adsorption-desorption isotherms (Tristar 3000, Micrometrics,) at 77 K, using the Barrett–Joyner–Halenda (BJH)

analysis for the desorption branch, the corresponding specific surface area was determined by the Brunauer–Emmett–Teller method (S_{BET}).

The 3D structures were imaged with a field emission scanning electron microscope (FE-SEM, S-4700; Hitachi) provided with an integrated energy dispersive spectroscopy (EDS) analyser. To evaluate the extent of the infiltration, line microanalyses were performed on representative samples (previously embedded in epoxy resin and diamond polished), using Proza correction and internal standards. In addition, 1400 X-ray images of one of the samples (the SiAl with double-infiltration) were taken with a CT-Scan (XT H-160, Nikon), to examine the homogeneity of the composite samples. High resolution transmission electron microscope (HRTEM, JEOL 2100) operating at 200 KV was used to observe in detail the hybrid samples. The TEM specimens were prepared by crushing and dispersing a small portion (20 mg) of the structures in isopropyl alcohol under sonication for 10 minutes, and then casting a drop with a micropipette on the TEM grid that was air-dried before observation.

For gaining knowledge about actual bonds and phases in the hybrid structures, Fourier transformed infrared spectroscopy with attenuated total reflectance (FTIR-ATR, Spectrum 100 spectrometer, Perkin Elmer) analyses were performed in transmittance mode (spectral range of 4000–400 cm^{-1}). Besides, Raman point analysis (Alpha 300-R, WITec) were done on SiO_2 and SiAl coatings on flat Si wafers after spreading the corresponding sol and gelling (AVT), similarly as it was done for the infiltrated structures. In this way, vibrations corresponding to the silica and silicoaluminate gels were directly identified since the strong Raman signal of graphitic species did not interfere in the spectra.

The hybrid scaffolds (SiO_2 and SiAl) were compression tested for both the single and double infiltrated structures, using a universal testing machine (ZwickiLine Z5.0TS,

Zwick-Roell). Test samples of dimensions 11.5 x 11.5 x 4.5 (in mm) were smoothly flattened using SiC grinding paper at the top/bottom surfaces (square-side) to guarantee a homogeneous load distribution. A preload of 3 N was applied to assure good contact, and a constant displacement rate of 0.5 $mm \cdot min^{-1}$ was applied until failure was detected by a rapid decrease in the load. Nominal stress was estimated dividing the load by the contact surface, and corresponding apparent strain data were calculated from the recorded platen displacement divided by the initial specimen height at pre-load. Strength was calculated from the maximum load achieved in each test, averaging data from a minimum of three samples per condition. Elastic modulus of each structure type was estimated from the stress-strain plots within the lineal-elastic regime.

The electrical conductivity of the structures was calculated at room temperature by a d.c. procedure. The four point method was used as in previous works [13], painting four silver paste electrodes (Electrolube, ERSCP03B), two on the outer faces of the scaffold and the other two on two in-plane rods separated ~ 4 mm. Different voltages in the range 100-500 mV were applied to the external electrodes (V_{ap}) by means of a d.c. source (Agilent E3646A) and the electrical current flowing through the system (I) was determined by a multimeter located in series (Keysight 34461A). The voltage between the inner electrodes (V) was measured by means of another independent multimeter (Agilent 34401A), and the corresponding electrical resistance was calculated by the linear regression of the I-V data. The electrical conductivity was calculated according to the expression $\sigma_e = \frac{L}{R*S}$, where *L* is the distance between the two inner electrodes, *R* is the measured resistance and *S* is the outer electrode surface.

3. Results and discussion

A problem that may occur when using the sol-gel route for the silica synthesis is the build-up of tensile stresses, which normally appear during the gel cross-linking and later thermal treatment [44], damaging the essentially delicate 3D rGO template as it is evidenced in Fig. 2a. Comparing the images of the original rGO scaffold and the silica sol infiltrated and thermally cured sample (Fig. 2b, c), the existence of an easily spalling layer is evidenced in the later. In contrast, the AVT induces the gel condensation by increasing the ambient pH but also reduces contraction stresses [45,46]; accordingly, a mostly continuous well attached covering of the rGO filaments is achieved with this process (Fig 2d), which stands out as a very convenient alternative for developing 3D silica-rGO hybrid structures. Besides, these composite structures truly reproduce the architecture of the original rGO scaffold, as seen in Fig. 2e by the 3D tomography of the AVT-treated rGO/SiAl_x2 sample, only detecting the non-carbonaceous components. The xerogel penetration is homogenous in the entire structure, independently of the location or the plane section (Fig. 2f), and similar filling is detected for the vertical (Figs. 2g, h) and horizontal filaments (Figs. 2i, j). Certain gel accumulation was only observed at some joints of filaments with the outer frame, thus this region was prone to cracking on gelling (see Supplementary Information S1).

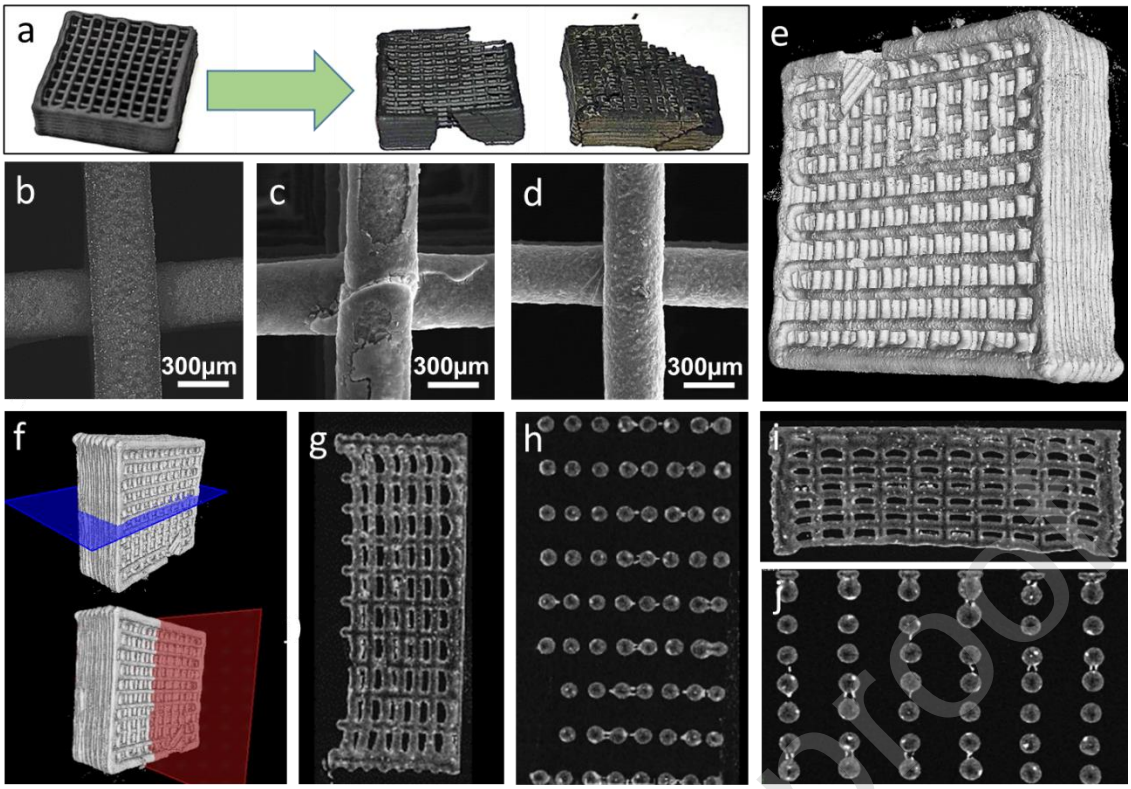

Figure 2. Pictures of a rGO scaffold (left image), and the same sample (top and bottom views) after SiO_2 sol infiltration (rGO/SiO_2_x1) and thermal curing (at 200 °C) (a); corresponding SEM images of the bare rGO scaffold (b), after silica infiltration and thermal curing (c), and after AVT gelling (d); tomographic image of a AVT cured rGO/SiAl_x2 structure (e), scaffold tomographic constructions depicting sectioning planes (f) for the vertical (g,h) and horizontal (i,j) scaffold projections at two magnification.

SEM images also indicate that the original rGO (Fig. 3a) and hybrid scaffolds (Fig. 3b,d) exhibit rods of a relatively smooth appearance, although after the second infiltration (x2 series) the presence of some texturing and even precipitates is detected on some filaments (Fig. 3c,e). Higher magnification images of the rod inside (Fig. 4 a-c) reveal the semitransparency of the rGO sheets in this structure, in contrast, a slight veil covering the

nanosheets is noticed for the hybrid structures, clearly associated to the network of fine particles typical dried gels (Fig. 4b,c). This fine silica-based covering has an important influence on the wetting characteristics of the structures. In fact, they become totally hydrophilic in contrast to the rGO scaffold and also develop an improved water adsorption capacity (about 10 times more), as can be seen in detail in the Supplementary information (S2). Even more, a surprising resistance against the attack of a high temperature direct flame is observed in the hybrids as well (see Supplementary Information S3)

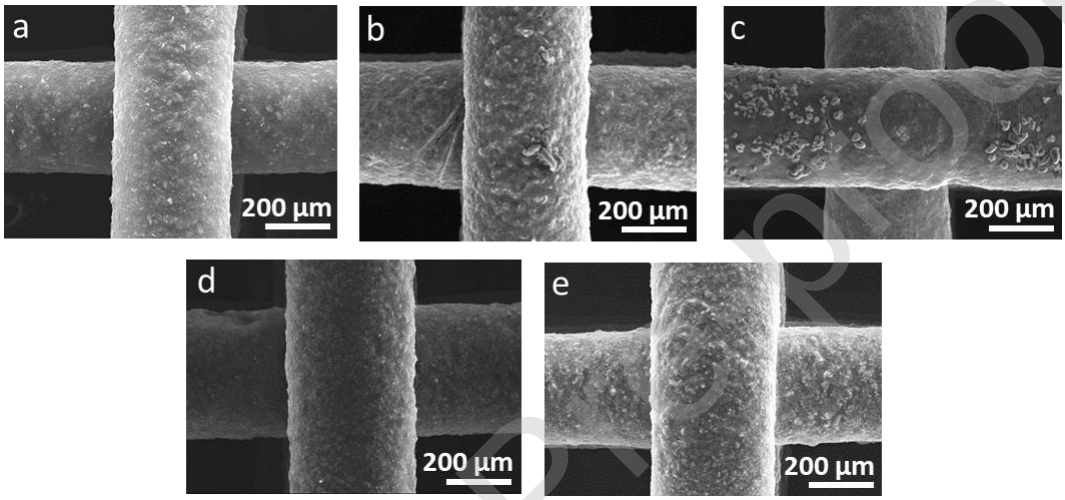

Figure 3. Comparing SEM images of the different materials, the original rGO scaffold (a), rGO/SiO_2_x1 (b), rGO/SiO_2_x2 (c), rGO/SiAl_x1 (d) and rGO/SiAl_x2 (e).

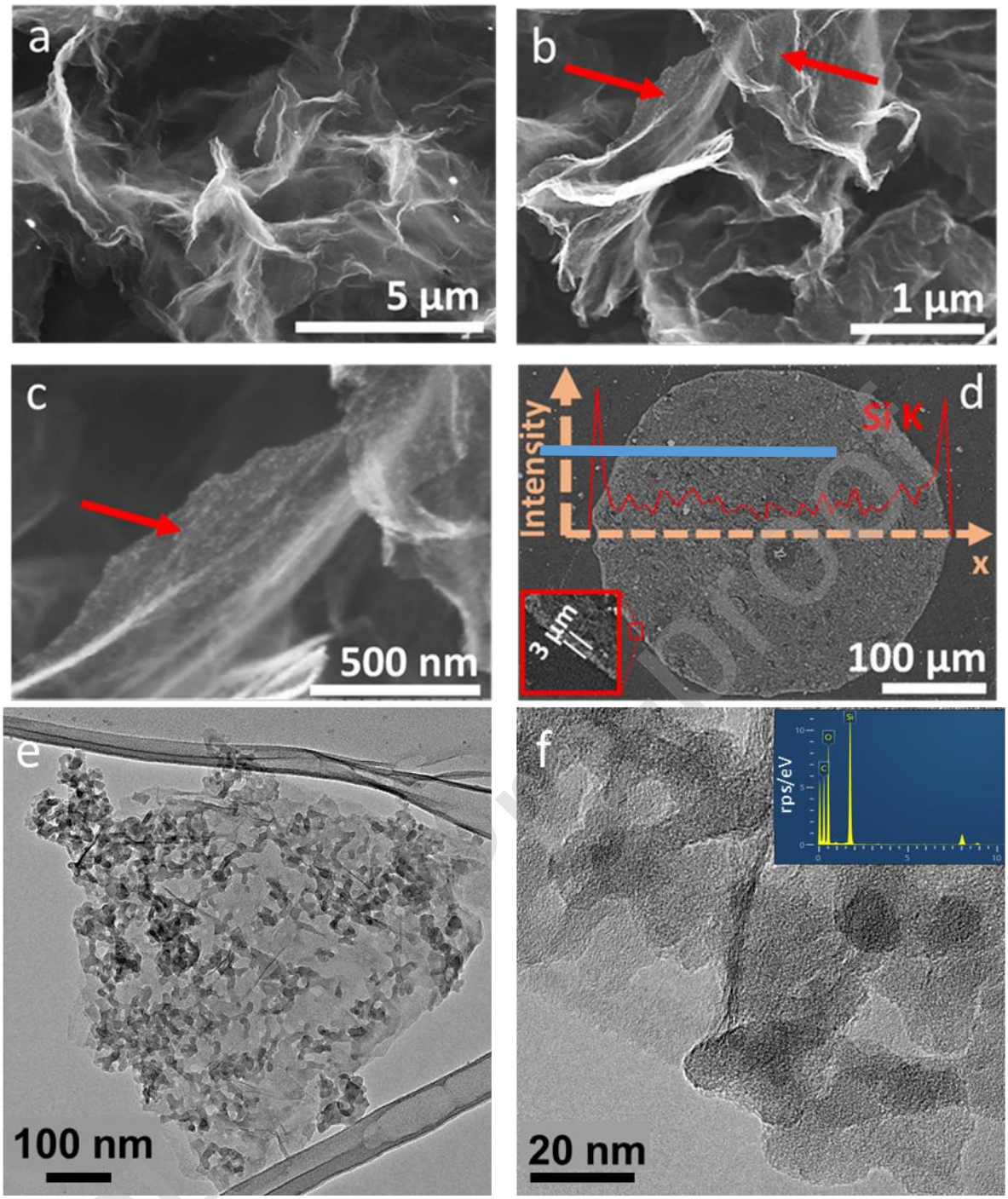

Figure 4. SEM images of rGO (a) and rGO/SiAl_x1 (b) rods; higher magnification view of the previous picture pointing to the slight veil of silica over the rGO platelets (c); SEM image of a rGO/SiO_2_x1 rod (polished cross-section) with superimposed EDS Si line profile (d); TEM general view of the xerogel network covering the GO sheet for

rGO/SiO2_x1 (e) and HRTEM image revealing the silica particles with the attached EDS microanalysis of the region (f).

The EDS line profile of Si (Si-K) performed on the polished cross-section of an rGO/SiO_2_x1 rod shows an almost constant on average sawtooth contour through the rod, except by the prominent increase of the Si signal near the rim that extends over a ~ 3 μm thick circular crown (Fig. 4d). This silica rich shell accounts for ~12 vol. % of the total silica xerogel volume in the structure, estimated by assuming a constant thickness of the silica rich rim (including rods and frame). The HRTEM images of the rGO/SiO2_x1 sample confirm the covering of the rGO sheets by the connected xerogel particles that spread uniformly over the rGO (Fig. 4e). The silica particles present a roundish elongated appearance with size the order of ~20 nm where the Si signal is detected by the EDS microanalysis (Fig. 4f). Results for the rGO/SiAl_x1 material are provided in the Supplementary Information (S6) showing similar characteristics except by the presence of Al EDS microanalysis.

Table 2. Geometrical parameters for the hybrid scaffolds: D, rod diameter, L, the length and H, the height. In parenthesis are the corresponding standard deviations

Structure	**L [mm]**	**H [mm]**	**D [μm]**
rGO/SiO_2_x1	11.5 (0.3)	4.5 (0.2)	380 (10)
rGO/SiO_2_x2	11.5 (0.3)	4.5 (0.3)	380 (5)
rGO/SiO_2_x1	11.6 (0.4)	4.5 (0.2)	375 (10)
rGO/SiAl_x2	11.6 (0.3)	4.5 (0.3)	375 (15)

In consonance with previous data [30], printed GO cuboids experience a linear shrinkage of ~2.5 % after the 1200 °C thermal reduction , displaying an average geometrical density (ρ_{geo}) of 0.03 ± 0.01 g·cm^{-3} and a porosity of the solid skeleton of 95 %, estimated from the theoretical density of rGO (2.2 g·cm^{-3}) [47]. The high porosity of the rGO rods certainly favours the solution infiltration through the capillary effect (see Supplementary Information S4 for an estimation of the capillary rise in the scaffold). Actually, the rGO structure increased up to 13 times its weight once removed from the solution, which corresponds to a sol volume of ~300 mm^3 that is practically equal to the skeleton volume (the calculation is detailed in Supplementary Information S5), which is consistent with the fact that the rGO network accounts just for ~5% of that volume. This result indicates that the infiltrating solution practically fills in the scaffold irrespectively of the type of sol (SiO_2 or SiAl). After infiltration and gel curing, the scaffolds maintain their dimensions since the typical diameter of filaments are very similar for both gels and persist unchanged even after a second infiltration (Table 2). Consequently, the development of potentially damaging stresses has been avoided. It is astonishing to observe how the xerogel replica still supports itself after removing the graphitic template by subjecting the structures to a treatment of 450 ºC in air for 2 h (Fig. 5). The calcined structures become white (Fig. 5a) and are formed by partially sintered silica grains of viscous appearance as displayed in the higher microstructure of Fig. 5b, hence, this provides an indirect method of getting structured porous silica scaffolds

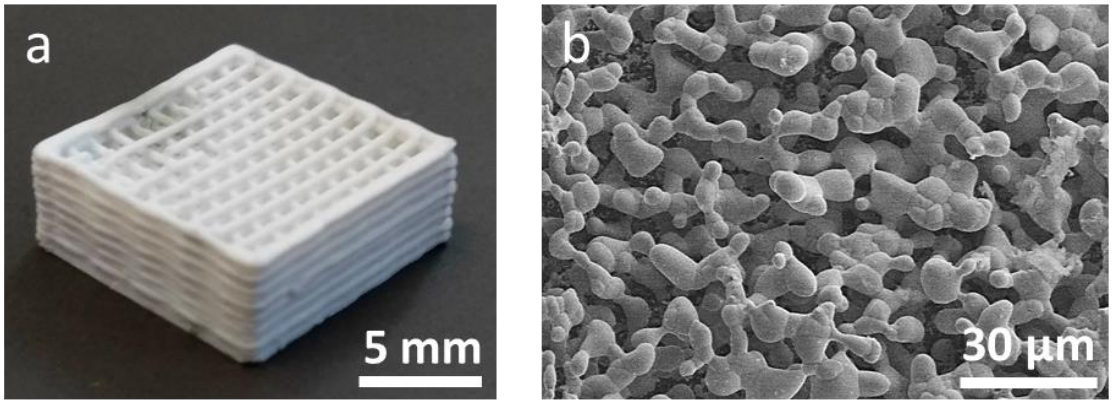

Figure 5. Image of a silica 3D rGO/SiO_x1 scaffold after calcination of the carbonaceous elements (a) and SEM image of the microstructure showing sintered silica particles (b).

The geometric density of the composite structures increases between 3 and 5 times (after consecutive infiltrations) when compared to ρ_{geo} of the unfilled rGO scaffold (Table 3), nonetheless, all the structures remain lightweight with $\rho_{geo} \leq 0.15$ g·cm^{-3}. The total porosity (Π_t) (Table 3) was calculated by comparing the geometric density to the theoretical ρ estimates for each hybrid structure, bearing in mind the theoretical density values of 2.2 g·cm^{-3} for rGO [47], 2.2 g·cm^{-3} for pure SiO_2 glass [48] and 2.4 g·cm^{-3} for the SiAl gel (see Supplementary Information S7 for the density calculation in the latter case) and the corresponding phase volume fractions (Table 3). The Π_t of the hybrid scaffolds stays in the range 94 - 97%, i.e. just a few points below that of the rGO structure (98%), slightly decreasing with the second infiltration but showing similar numbers for both gels.

Table 3. Values of geometric density (ρ_{geo}), skeleton density (ρ_{rod}) total porosity (Π_t), rod porosity (Π_{rod}) with standard deviation (Δ) and the mass and volume percentages of xerogel (silica or Al-modified silica) for the respective infiltrations

Structure	**Impregnations**	**ρ_{geo} ($g \cdot cm^{-3}$) (Δ=10%)**	**ρ_{rod} ($g \cdot cm^{-3}$) (Δ=10%)**	**xerogel (wt. %)**	**xerogel (vol. %)**	**Π_t (%)**	**Π_{rod} (%)**
rGO platform	-	0.03	0.1	-	-	~98	~96
SiO_2	x1	0.09	0.1	50 ± 4	50 ± 4	~97	~94
	x2	0.15	0.3	75 ± 5	75 ± 5	~94	~89
SiAl	x1	0.09	0.2	55 ± 4	52 ± 4	~96	~92
	x2	0.14	0.3	82 ± 5	77 ± 5	~94	~89

The porosity of the skeletons (Π_{rod}) was calculated by the equation $\Pi_{rod} = \left(\frac{\Pi_t - \Pi_{CAD}}{1-\Pi_{CAD}}\right)$, in which Π_{CAD} refers to the porosity of the rGO scaffold design (46 - 48%) as calculated by the expression $\Pi_{CAD} = \left(1 - \frac{\pi\phi^2}{2ah} - \frac{Vext}{V\_total}\right)$ [49,50], where ϕ is the rod diameter, *a*, the in-plane rod gap, *h* is the vertical distance between contiguous rods, V_{ext} is the frame volume and V_{total} is the outer volume of the structure. Hence, Π_{rod} ranges from 89 to 94 % according to the number of infiltrations, which are figures about 2-7% lower than Π_{rod} of the rGO structure (Table 3). Although during the impregnation the solution fills up the available volume (open porosity) of the rGO skeleton, it should be considered when analysing the above Π_{rod} data that on drying, the gel reduces its volume as much as the volume of solvent used (i.e. water plus ethanol content ~75 %). Presently, the volume occupied by the xerogel represents ~ 25 % of the rod volume at the most, ignoring the gel densification [51], which is probable dimmed because the room temperature nature of the

AVT process and perhaps affected by the GO support, as reported for different gel derived silica composites [52,53].

It is relevant to analyse in detail the type of porosity of the present hybrid structures. Pore size distributions are represented in Fig. 6a,b for rGO/SiO_2_x1 and rGO/SiAl_x1 respectively, and also for the original rGO (Fig. 6c). The occurrence of mesoporous that peak at ~ 45 nm is evidenced in all the structures;, at the same time, the incidence of certain mesoporosity around 2 – 4 nm is confirmed as seen by the insets of Fig. 6. Total pore volumes of 1.40 ± 0.02 (rGO/SiO_2_x1) and 0.70 ± 0.02 $cm^3 \cdot g^{-1}$ (rGO/SiAl_x1) are determined in the pore range of 2 – 60 nm while the original rGO scaffold presents a total pore volume of 0.50 ± 0.02 $cm^3 \cdot g^{-1}$ for the same pore range.

The occurrence of both micro- and meso-porosity has been proved for various SiO_2 hybrid systems processed by the sol-gel method, such as in porous ZrO_2 ceramics impregnated with a TEOS solution [54], and focusing on nano-carbons, the early example of a surfactant intercalated graphite oxide immersed in a TEOS solution [55]. The pore size distribution in the silica containing hybrid essentially depends on parameters such as the temperature, pH and pressure employed during the polymerisation and condensation stages of the silica precursor [56,57], this conversion process is often accompanied by the development of quite high S_{BET}. In particular, silica-GO composite aerogels with S_{BET} in the range 676-846 $m^2 \cdot g^{-1}$ are reported for composites synthesized via hydrothermal reactions (at 120 ºC) and after thermal treatments at 790 ºC, or using large amount of hazardous products such n-hexane [33,58]. In contrast, the present method uses an easy infiltration route and mostly room temperature procedures.

The actual 3D hybrid samples exhibit S_{BET} values of 350 and 300 $m^2 \cdot g^{-1}$ (± 3%) for rGO/SiO_2_x1 and rGO/SiAl_x1, respectively, which are above the S_{BET} of the used rGO

template (125 $m^2 \cdot g^{-1}$); hence, this increment can be attributed to the mesoporous silica or SiAl xerogels covering the rGO nanostructures. The lower S_{BET} measured for the rGO/SiAl_x1 structure runs parallel to the experienced by Al modified bulk silica gels respect to pure silica gels [59].

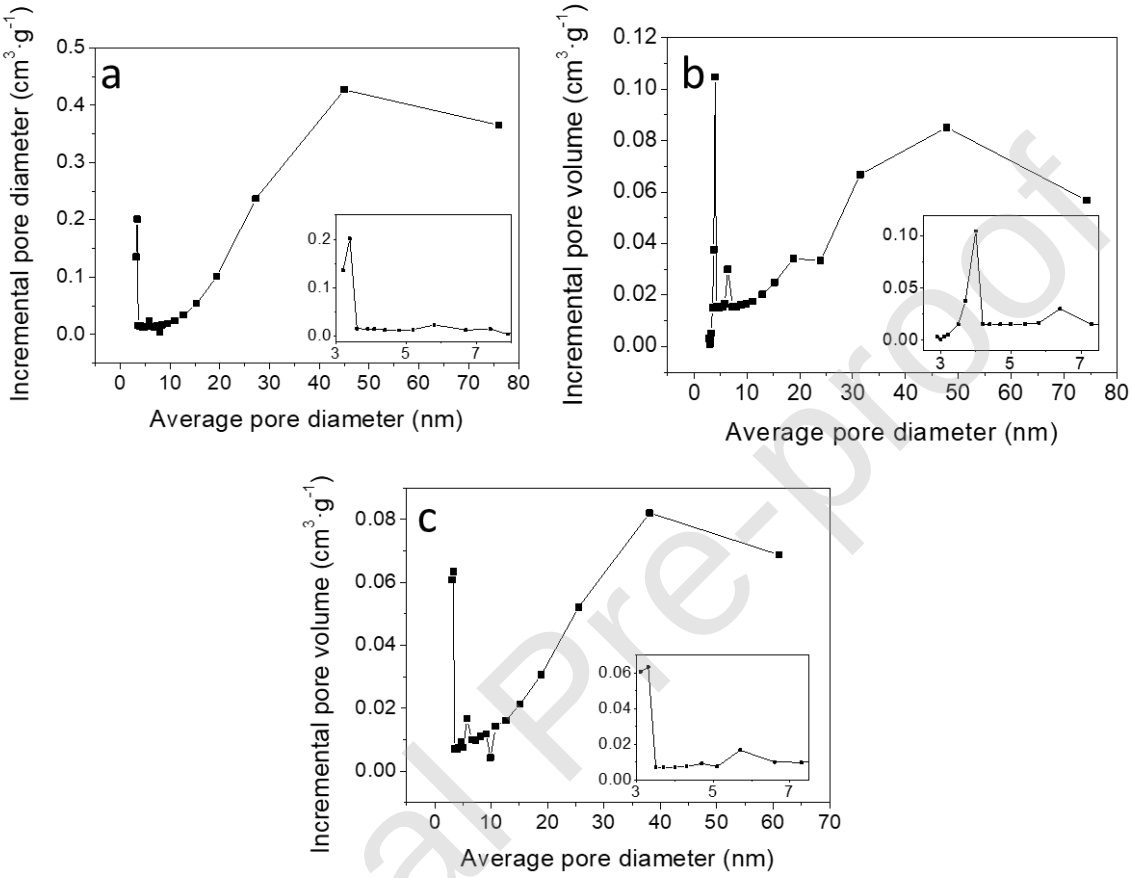

Figure 6. Pore size distribution from nitrogen absorption-desorption analysis of rGO/SiO_2_x1 (a), rGO/SiAl_x1 (b) and uncoated rGO (c) structures.

The FTIR spectra of the present hybrids permitted the identification of typical bands for silica (Fig. 7), in particular, the intense absorption band at 1067 cm^{-1} associated to Si-O-Si and Si-O-C groups also [58]. The smaller peaks at 440 cm^{-1} and 570 cm^{-1} are attributed Si-O-Si bonds, and also the small band at 790 cm^{-1} due of the Si-O bond [60], which some authors associate to a the interaction between silica and rGO (Si-O-C) [33]. The wide

band in the region 4000-3000 cm^{-1} distinguished in some of the spectra corresponds to stretching vibrations of O-H groups due to constitutional water. As for the Si-Al hybrid, a certain shift of the intense 1060 cm^{-1} peak towards lower wavenumbers is perceived when compared to the silica/rGO spectrum (Fig. 7), which could be affected by the intense shoulder at the lower wavenumber side of the 1060 cm^{-1} peak, which has been related to Si-O-Al vibrations by some authors [59]. Besides, the small peaks at 600 and 636 cm^{-1} could be attributed to Al-O bonds with octahedral coordination [61,62]. Smaller peaks corresponding to the graphitic phase are also observed in the hybrids, which can be compared to the spectrum of the rGO alone that shows relatively lower intensity than the previous hybrid materials and displays a wide band around 1220-800 cm^{-1} due to C–O bonds, a band around 1460-1573 cm^{-1} that coincides with regions of C-OH and C=O vibrations, and finally a band at 1760 cm^{-1} typical of the carbonyl group [63].

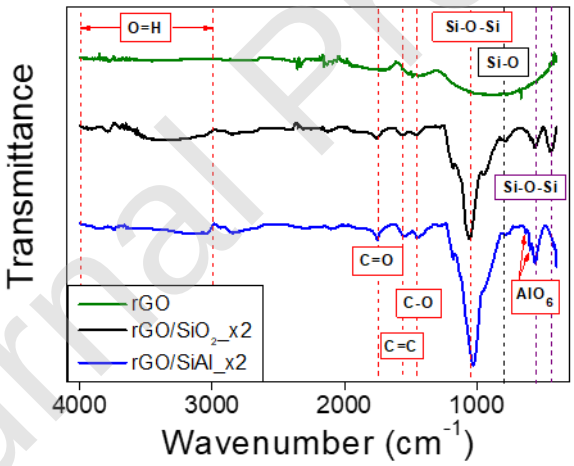

Figure 7. FTIR spectra of rGO, rGO/SiO_2_x2 and rGO/SiAl_x2 structures. Main peaks and regions are marked in the spectra.

Two zones are discriminated in the Raman point spectrum of the SiO_2 coating at low (600 - 1100 cm^{-1}) and high (2500 – 4000 cm^{-1}) Raman shifts (Fig. 8a). Applying a peak

deconvolution tool separately for each region, characteristic bands of SiO_2 gels [64] are identified at 811, 885, 940, 969 and 1020 cm^{-1} in the low displacement region (Fig. 8b), and wider bands at 3214, 3469 and 3613 cm^{-1} for the high displacement zone (Fig. 8c). The SiAl gel coating also shows two distinctive zones (Fig. 8d) with similar peaks to those identified for the SiO_2 coating at low displacements; whereas in the 250 – 4000 cm^{-1} region, apart from the silica peaks, different bands identified with aluminium hydroxides (gibbsite and bayerite) and oxyhydroxide (boehmite) [65] are revealed (Fig. 8e). Corresponding peaks are at 3381, 3529 and 3615 cm^{-1} (gibbsite), 3420, 348, 3450 and 3668 cm^{-1} (bayerite) and 2988, 3045, 3214 and 3365 cm^{-1} (boehmite). Based on the FTIR and Raman results, the samples impregnated with the SiAl sol show no evidence of atomic interaction between SiO_2 and Al_2O_3 units, which is common in aluminosilicate gels that have not been treated at high temperatures or lack of atomic level homogeneity [66,67]. On the other hand, it has been proposed that in wet aluminosilicate gels connection between Si and Al ions preferably occur by OH links (Al-OH-Al/Si groups), which are not detected because overlapping with other bands [68].

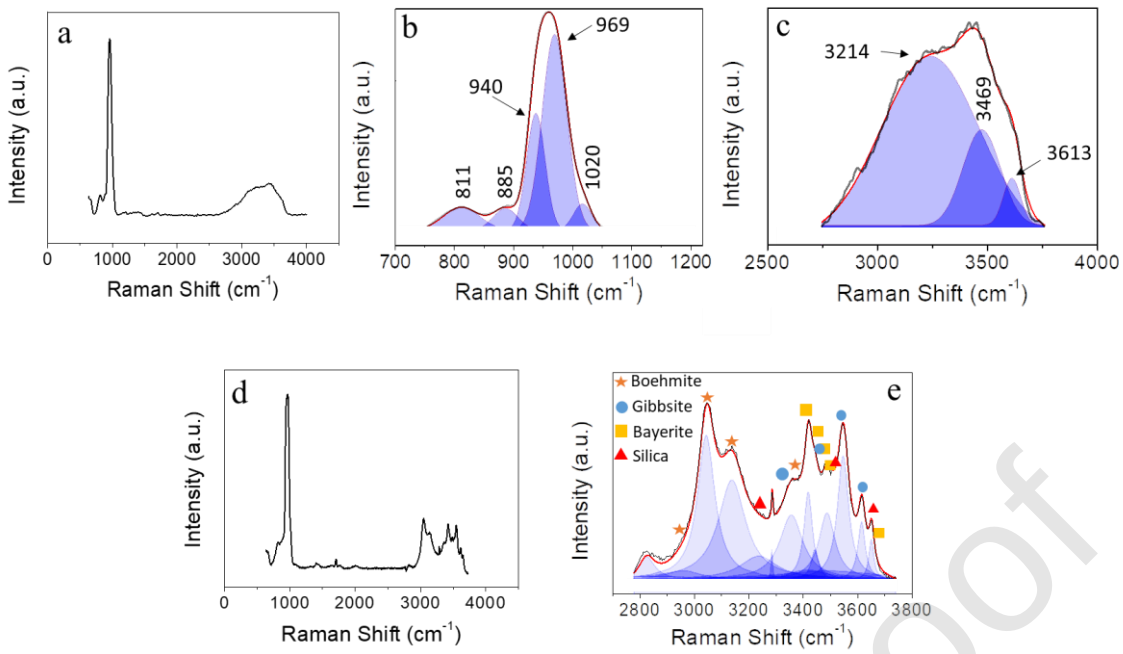

Figure 8. Point Raman spectrum of the SiO_2 treated gel (a), and corresponding peak deconvolutions at low (b) and high (c) Raman displacements; alike point Raman spectrum of SiAl coating (d), and peak deconvolution plot with the ascribed phases (boehmite, gibbsite, bayerite and silica) (e).

Representative loading curves for the different structures (rGO and hybrids) are compared in Figure 9a, all showing a gradual collapse of the structure after reaching the peak stress, which is common in fragile cellular materials [69]. Silica-containing structures experience a noticeable improvement in strength, one order of magnitude over bare rGO scaffold, and a relative improvement after the second infiltration as well. Therefore, it is evident that the interaction between both networks (rGO and silica) actually provides stronger structures than any of them separately. The SiAl gel also generates a significant increase in resistance for the rGO structure, particularly after the second infiltration (Fig. 9a). This effect may be due to certain strengthening of the silica gel network by the Al atoms. Although Al being mostly in octahedral coordination with bridging O^{2-} and acting

as a network modifier of the silica gel network, however, a certain amount of tetrahedral $[AlO_4]^{4-}$ replacing Si ions is probable, in a similar way as occurs in silicoaluminate glass [70,71]. This phenomenon induces important modification of the glass network to maintain charge neutrality, for example, decreasing the amount of non-bridging $[OH^-]$ /$[O^{2-}]$ groups, which affects the glass properties as eliminates weaker links [71].

The average strength of the hybrids and bare rGO structures is plotted in Fig. 9b, together with published data for some illustrative cellular materials, such as alumina-carbon aerogels [72], mullite foams [73-74], silica foams [75-76], and GO-silica aerogels [41,42] and foams [33]. The present 3D composite structures with strengths in the range 100 to 400 kPa compare very favourably with cellular materials of alike composition and density [33,42].

The apparent elastic moduli (E) are compared for the present 3D structures in Fig 9c, displaying similar trend to the corresponding strength data (Fig. 9a), the stiffer structures being the SiAl/rGO. Elastic modulus of the hybrid structures is between 1 – 2 orders of magnitude higher than the corresponding E of bare GO template, and proportional to the silica (or Al modified silica) content as well. A parallel effect can be seen in E of SiO_2 glass when introducing $[AlO4]^{4-}$ units in the network attributed to the better atomic packing, which is a proved elastic modulus enhancer within a particular glass family [77]. The elastic moduli of present 3D hybrid structures range between 3 and 13 MPa, and can be contrasted with the E of 0.07 MPa reported for a silica-GO aerogel with 40 wt.% GO and density of 0.015 $g \cdot cm^{-3}$ [78] or the value of 0.4 MPa referred for a porous silica-GO material with a 5 wt.% of GO and a density of 0.15 $g \cdot cm^{-3}$ [42].

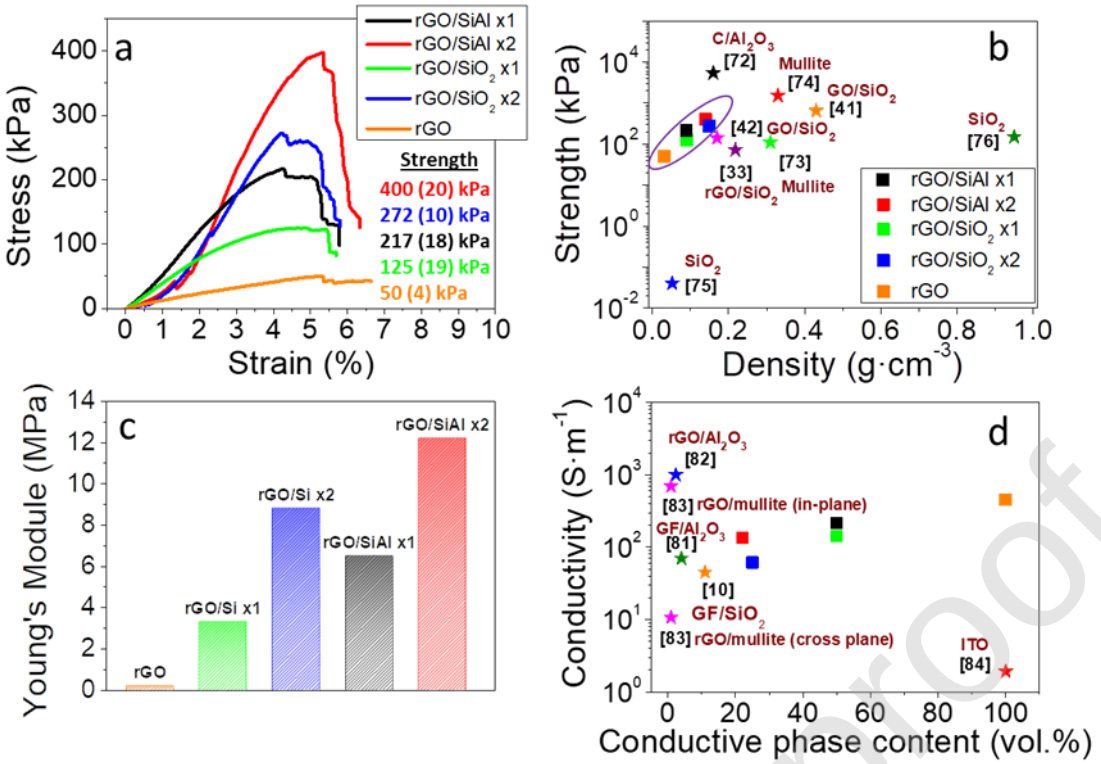

Figure 9. Comparison of the stress-strain curves of each structure (a); average compression strength for present materials (squares) and representative data for several 3D cellular structures with corresponding references in brackets (b); apparent elastic moduli of the bare and composite structures (c); and electrical conductivity vs. the conductive phase content (vol.%) of the developed materials plotted with reported data for dense ceramic composites (d).

The hybrid structures demonstrate high electrical conductivity (σ) figures, in the range 60 – 215 S·m^{-1} (Fig. 9c), lower of course than σ of the 3D rGO (480 S·m^{-1}), and showing an inverse relation to the content of insulating phases. The conductivity of a single rod (σ_{rod}) can be estimated by the equation $\sigma_{rod} = \frac{2a}{\phi}\sigma$, applicable for an unidirectional current flow along the rod axis, as stated in a previous work [49], resulting in σ_{rod} values of 840

– 360 $S \cdot m^{-1}$ for rGO/SiO_2, and 1260 – 800 $S \cdot m^{-1}$ for rGO/SiAl, the lower values of each set pertaining to the second infiltration.

We can contrast the conductivity of present hybrids with published σ data for dense graphene containing composites of silica [10], alumina [81,82] and mullite [83] (Fig. 9d). Specifically, thin films of silica with graphene nanoplatelets (11 vol. %) [10] show σ of 45 $S \cdot m^{-1}$, alumina with 4 vol. % of graphene nanoplatelets displays 70 $S \cdot m^{-1}$ [81] but reaches 10^3 $S \cdot m^{-1}$ for a composite with rGO (2.4 vol, %) prepared by a colloidal route [82], whereas a mullite/rGO (0.89 vol.%) composite fabricated from γ-Al_2O_3 and TEOS displays highly anisotropic electrical conductivity with values as high as 696 $S \cdot m^{-1}$ for the in-plane and ~11 $S \cdot m^{-1}$ for the cross-plane direction [83]. By way of comparison, a aerogel of pure indium-tin-oxide treated at 600ºC [84], a well-known conductive oxide widely used in electronic devices, presents an electrical conductivity of ~2 $S \cdot m^{-1}$. Accordingly, the 3D silica-rGO hybrids developed exhibit very competitive conductivity values considering their low density.

4. Conclusions

3D rGO composite structures are prepared by infiltrating 3D rGO printed structures with both silica and silica-alumina precursors via a room temperature sol-gel route, which replicates the shape of the rGO platform. These hybrid structures (20-50 wt. % rGO) remain highly porous (~94%), exhibit an increment of the specific surface area of up to 100 % (referred to the rGO structure) and a predominance of mesoporores (45 nm size). The compression strength increases between 250 – 800 % in the hybrids respect to both silica xerogels and 3D rGO, respectively, while maintain significant electrical conductivities for the 3D scaffolds (61.5 – 214 $S \cdot m^{-1}$) and filaments (360 a 1260 $S \cdot m^{-1}$).

The marked hydrophilic nature and considerable capacity for water absorption are additional merits of the hybrid structures. The enhanced performance of the hybrids besides the advantage of the room temperature procedure suggest that these materials would be of potential interest as absorbers, pollutants removal, gas sensing and thermal storage or photocatalytic water splitting applications.

Declaration of interests

The authors declare that they have no known competing financial interests or personal relationships that could have appeared to influence the work reported in this paper.

Acknowledgements

This work was supported by Spanish project RTI2018-095052-B-I00 (MCIU/AEI, Spain and FEDER, UE). JJM acknowledges the financial support of MCIU through the FPI contract ref: BES-2016-077759.

References

[1] D.A.C. Brownson, D.K. Kampouris, C.E. Banks, An overview of graphene in energy production and storage applications, J. Power Sources. 196 (2011) 4873–4885. https://doi.org/10.1016/j.jpowsour.2011.02.022.

[2] T. Palaniselvam, J.B. Baek, Graphene based 2D-materials for supercapacitors, 2D Mater. 2 (2015) 32002. https://doi.org/10.1088/2053-1583/2/3/032002.

[3] R. Sordan, F. Traversi, V. Russo, Logic gates with a single graphene transistor, Appl. Phys. Lett. 94 (2009). https://doi.org/10.1063/1.3079663.

[4] Y.M. Lin, A. Valdes-Garcia, S.J. Han, D.B. Farmer, I. Meric, Y. Sun, Y. Wu, C. Dimitrakopoulos, A. Grill, P. Avouris, K.A. Jenkins, Wafer-scale graphene

integrated circuit, Science (80-.). 332 (2011) 1294–1297. https://doi.org/10.1126/science.1204428.

[5] V. Dhinakaran, M. Lavanya, K. Vigneswari, M. Ravichandran, M.D. Vijayakumar, Review on exploration of graphene in diverse applications and its future horizon, Mater. Today Proc. (2020). https://doi.org/10.1016/j.matpr.2019.12.369.

[6] X. Yu, W. Zhang, P. Zhang, Z. Su, Fabrication technologies and sensing applications of graphene-based composite films: Advances and challenges, Biosens. Bioelectron. 89 (2017) 72–84. https://doi.org/10.1016/j.bios.2016.01.081.

[7] C. Mattevi, H. Kim, M. Chhowalla, A review of chemical vapour deposition of graphene on copper, J. Mater. Chem. 21 (2011) 3324–3334. https://doi.org/10.1039/c0jm02126a.

[8] C. Ramirez, P. Miranzo, M. Belmonte, M.I. Osendi, P. Poza, S.M. Vega-Diaz, M. Terrones, Extraordinary toughening enhancement and flexural strength in Si3N4 composites using graphene sheets, J. Eur. Ceram. Soc. 34 (2014) 161–169. https://doi.org/10.1016/j.jeurceramsoc.2013.08.039.

[9] M. Belmonte, C. Ramírez, J. González-Julián, J. Schneider, P. Miranzo, M.I. Osendi, The beneficial effect of graphene nanofillers on the tribological performance of ceramics, Carbon N. Y. 61 (2013) 431–435. https://doi.org/10.1016/j.carbon.2013.04.102.

[10] S. Watcharotone, D.A. Diking Sasha Stankovich, R. Pinery, I. Jung, G.H.B. Dommett, G. Evmenenko, S.E. Wu, S.F. Chen, C.P. Liu, S.T. Nguyen, R.S. Ruoff, Graphene-silica composite thin films as transparent conductors, Nano

Lett. 7 (2007) 1888–1892. https://doi.org/10.1021/nl070477+.

[11] H. Porwal, P. Tatarko, S. Grasso, C. Hu, A.R. Boccaccini, I. Dlouhý, M.J. Reece, Toughened and machinable glass matrix composites reinforced with graphene and graphene-oxide nano platelets, Sci. Technol. Adv. Mater. 14 (2013). https://doi.org/10.1088/1468-6996/14/5/055007.

[12] M.A. Worsley, P.J. Pauzauskie, T.Y. Olson, J. Biener, J.H. Satcher, T.F. Baumann, Synthesis of graphene aerogel with high electrical conductivity, J. Am. Chem. Soc. 132 (2010) 14067–14069. https://doi.org/10.1021/ja1072299.

[13] J.J. Moyano, A. Gómez-Gómez, D. Pérez-Coll, M. Belmonte, P. Miranzo, M.I. Osendi, Filament printing of graphene-based inks into self-supported 3D architectures, Carbon N. Y. 151 (2019) 94–102. https://doi.org/10.1016/j.carbon.2019.05.059.

[14] Y.A. Samad, Y. Li, A. Schiffer, S.M. Alhassan, K. Liao, Graphene foam developed with a novel two-step technique for low and high strains and pressure-sensing applications, Small. 11 (2015) 2380–2385. https://doi.org/10.1002/smll.201403532.

[15] E. García-Tuñon, S. Barg, J. Franco, R. Bell, S. Eslava, E. D'Elia, R.C. Maher, F. Guitian, E. Saiz, Printing in three dimensions with Graphene, Adv. Mater. 27 (2015) 1688–1693. https://doi.org/10.1002/adma.201405046.

[16] S. Drieschner, M. Weber, J. Wohlketzetter, J. Vieten, E. Makrygiannis, B.M. Blaschke, V. Morandi, L. Colombo, F. Bonaccorso, J.A. Garrido, High surface area graphene foams by chemical vapor deposition, 2D Mater. 3 (2016) 1–10. https://doi.org/10.1088/2053-1583/3/4/045013.

[17] Y. Ping, Y. Gong, Q. Fu, C. Pan, Preparation of three-dimensional graphene foam for high performance supercapacitors, Prog. Nat. Sci. Mater. Int. 27 (2017) 177–181. https://doi.org/10.1016/j.pnsc.2017.03.005.

[18] L. Lu, J.T.M. De Hosson, Y. Pei, Three-dimensional micron-porous graphene foams for lightweight current collectors of lithium-sulfur batteries, Carbon N. Y. 144 (2019) 713–723. https://doi.org/10.1016/j.carbon.2018.12.103.

[19] X. Huang, B. Sun, D. Su, D. Zhao, G. Wang, Soft-template synthesis of 3D porous graphene foams with tunable architectures for lithium-O2 batteries and oil adsorption applications, J. Mater. Chem. A. 2 (2014) 7973–7979. https://doi.org/10.1039/c4ta00829d.

[20] M. Horn, B. Gupta, J. MacLeod, J. Liu, N. Motta, Graphene-based supercapacitor electrodes: Addressing challenges in mechanisms and materials, Curr. Opin. Green Sustain. Chem. 17 (2019) 42–48. https://doi.org/10.1016/j.cogsc.2019.03.004.

[21] U. Patil, S.C. Lee, S. Kulkarni, J.S. Sohn, M.S. Nam, S. Han, S.C. Jun, Nanostructured pseudocapacitive materials decorated 3D graphene foam electrodes for next generation supercapacitors, Nanoscale. 7 (2015) 6999–7021. https://doi.org/10.1039/c5nr01135c.

[22] C. Huang, C. Li, G. Shi, Graphene based catalysts, Energy Environ. Sci. 5 (2012) 8848–8868. https://doi.org/10.1039/c2ee22238h.

[23] A. Quintanilla, J. Carbajo, J.A. Casas, P. Miranzo, M.I. Osendi, M. Belmonte, Graphene-based nanostructures as catalysts for wet peroxide oxidation treatments: From nanopowders to 3D printed porous monoliths, Catal. Today. (2019) 0–1. https://doi.org/10.1016/j.cattod.2019.06.026.

[24] X. Wang, R. Yin, L. Zeng, M. Zhu, A review of graphene-based nanomaterials for removal of antibiotics from aqueous environments, Environ. Pollut. 253 (2019) 100–110. https://doi.org/10.1016/j.envpol.2019.06.067.

[25] D. Chakravarty, C.S. Tiwary, C.F. Woellner, S. Radhakrishnan, S. Vinod, S. Ozden, P.A. da Silva Autreto, S. Bhowmick, S. Asif, S.A. Mani, D.S. Galvao, P.M. Ajayan, 3D Porous Graphene by Low-Temperature Plasma Welding for Bone Implants, Adv. Mater. 28 (2016) 8959–8967. https://doi.org/10.1002/adma.201603146.

[26] Y.W. Chen, Y.L. Su, S.H. Hu, S.Y. Chen, Functionalized graphene nanocomposites for enhancing photothermal therapy in tumor treatment, Adv. Drug Deliv. Rev. 105 (2016) 190–204. https://doi.org/10.1016/j.addr.2016.05.022.

[27] L. Wang, H. Liu, X. Lv, G. Cui, G. Gu, Facile synthesis 3D porous MXene Ti3C2Tx@RGO composite aerogel with excellent dielectric loss and electromagnetic wave absorption, J. Alloys Compd. 828 (2020) 154251. https://doi.org/10.1016/j.jallcom.2020.154251.

[28] S. Chen, S.Z. Qiao, Hierarchically porous nitrogen-doped graphene-NiCo2O4 Hybrid Paper as an advanced electrocatalytic water-splitting material, ACS Nano. 7 (2013) 10190–10196. https://doi.org/10.1021/nn404444r.

[29] G. Hu, C. Xu, Z. Sun, S. Wang, H.M. Cheng, F. Li, W. Ren, 3D Graphene-Foam-Reduced-Graphene-Oxide Hybrid Nested Hierarchical Networks for High-Performance Li-S Batteries, Adv. Mater. 28 (2016) 1603–1609. https://doi.org/10.1002/adma.201504765.

[30] J.J. Moyano, J. Mosa, M. Aparicio, D. Pérez-Coll, M. Belmonte, P. Miranzo,

M.I. Osendi, Strong and light cellular silicon carbonitride – reduced graphene oxide material with enhanced electrical conductivity and capacitive response, Addit. Manuf. 30 (2019) 100849. https://doi.org/10.1016/j.addma.2019.100849.

[31] J.J. Moyano, I. Garcia, J. De Damborenea, D. Pérez-Coll, M. Belmonte, P. Miranzo, M.I. Osendi, Remarkable Effects of an Electrodeposited Copper Skin on the 2 Strength and the Electrical and Thermal Conductivities of Reduced 3 Graphene Oxide-Printed Scaffold, ACS Appl. Mater. Interfaces. (2020). https://doi.org/10.1021/acsami.0c01819.

[32] Z.S. Wu, Y. Sun, Y.Z. Tan, S. Yang, X. Feng, K. Müllen, Three-dimensional graphene-based macro- and mesoporous frameworks for high-performance electrochemical capacitive energy storage, J. Am. Chem. Soc. 134 (2012) 19532–19535. https://doi.org/10.1021/ja308676h.

[33] X. Zhao, Y. Zhu, Y. Wang, Z. Li, Y. Sun, S. Zhao, X. Wu, D. Cao, Hydrophobic, blocky silica-reduced graphene oxide hybrid sponges as highly efficient and recyclable sorbents, Appl. Surf. Sci. 486 (2019) 303–311. https://doi.org/10.1016/j.apsusc.2019.05.017.

[34] X. Zhou, T. Shi, One-pot hydrothermal synthesis of a mesoporous SiO 2 - graphene hybrid with tunable surface area and pore size, Appl. Surf. Sci. 259 (2012) 566–573. https://doi.org/10.1016/j.apsusc.2012.06.113.

[35] S.V. Thakkar, A. Pinna, C.M. Carbonaro, L. Malfatti, P. Guardia, A. Cabot, M.F. Casula, Performance of oil sorbents based on reduced graphene oxide-silica composite aerogels, J. Environ. Chem. Eng. 8 (2020) 103632. https://doi.org/10.1016/j.jece.2019.103632.

[36] Y. chen Du, L. jun Huang, Y. xin Wang, K. Yang, Z. jie Zhang, Y. Wang, M.J.

Kipper, L.A. Belfiore, J. guo Tang, Preparation of graphene oxide/silica hybrid composite membranes and performance studies in water treatment, J. Mater. Sci. (2020). https://doi.org/10.1007/s10853-020-04774-5.

[37] L. He, S. Mo, P. Lin, L. Jia, Y. Chen, Z. Cheng, D-mannitol@silica/graphene oxide nanoencapsulated phase change material with high phase change properties and thermal reliability, Appl. Energy. 268 (2020) 115020. https://doi.org/10.1016/j.apenergy.2020.115020.

[38] L. Kou, C. Gao, Making silica nanoparticle-covered graphene oxide nanohybrids as general building blocks for large-area superhydrophilic coatings, Nanoscale. 3 (2011) 519–528. https://doi.org/10.1039/c0nr00609b.

[39] S. Karamikamkar, H.E. Naguib, C.B. Park, Advances in precursor system for silica-based aerogel production toward improved mechanical properties, customized morphology, and multifunctionality: A review, Adv. Colloid Interface Sci. 276 (2020) 102101. https://doi.org/10.1016/j.cis.2020.102101.

[40] G. Zu, K. Kanamori, T. Shimizu, Y. Zhu, A. Maeno, H. Kaji, K. Nakanishi, J. Shen, Versatile Double-Cross-Linking Approach to Transparent, Machinable, Supercompressible, Highly bendable aerogel thermal superinsulators, Chem. Mater. 30 (2018) 2759–2770. https://doi.org/10.1021/acs.chemmater.8b00563.

[41] L. Hong-li, H. Xiang, L. Hong-yan, L. Jing, L. Ya-jing, Novel GO/silica composite aerogels with enhanced mechanical and thermal insulation properties prepared at ambient pressure, Ferroelectrics. 528 (2018) 15–21. https://doi.org/10.1080/00150193.2018.1448192.

[42] Y. Lei, Z. Hu, B. Cao, X. Chen, H. Song, Enhancements of thermal insulation and mechanical property of silica aerogel monoliths by mixing graphene oxide,

Mater. Chem. Phys. 187 (2017) 183–190. https://doi.org/10.1016/j.matchemphys.2016.11.064.

[43] M. Boudot, V. Gaud, M. Selmane, D. Grosso, Sol − Gel Based Hydrophobic Antireflective Coatings on Organic Substrates: A Detailed Investigation of Ammonia Vapor Treatment (AVT), (2014).

[44] L.. Hench, J.K. West, The Sol-Gel Process, Chem. Rev. 90 (1990) 33–72.

[45] M. Boudot, V. Gaud, M. Louarn, M. Selmane, D. Grosso, Sol-gel based hydrophobic antireflective coatings on organic substrates: A detailed investigation of ammonia vapor treatment (AVT), Chem. Mater. 26 (2014) 1822–1833. https://doi.org/10.1021/cm403787v.

[46] P.F. Belleville, H.G. Floch, Ammonia hardening of porous silica antireflective coatings, Sol-Gel Opt. III. 2288 (2004) 25. https://doi.org/10.1117/12.188957.

[47] J. Pappis, S.L. Blum, Properties of Pyrolytic Graphite, J. Am. Ceram. Soc. 44 (1961) 592–597. https://doi.org/10.1111/j.1151-2916.1961.tb11664.x.

[48] F.G. Araújo, G.P. LaTorre, L.L. Hench, Structural evolution of a porous type-VI sol-gel silica glass, J. Non. Cryst. Solids. 185 (1995) 41–48. https://doi.org/10.1016/0022-3093(94)00653-9.

[49] B. Román-Manso, F.M. Figueiredo, B. Achiaga, R. Barea, D. Pérez-Coll, A. Morelos-Gómez, M. Terrones, M.I. Osendi, M. Belmonte, P. Miranzo, Electrically functional 3D-architectured graphene/SiC composites, Carbon N. Y. 100 (2016) 318–328. https://doi.org/10.1016/j.carbon.2015.12.103.

[50] B. Román-Manso, J.J. Moyano, D. Pérez-Coll, M. Belmonte, P. Miranzo, M.I. Osendi, Polymer-derived ceramic/graphene oxide architected composite with

high electrical conductivity and enhanced thermal resistance, J. Eur. Ceram. Soc. 38 (2018) 2265–2271. https://doi.org/10.1016/j.jeurceramsoc.2017.12.060.

[51] I. Strawbridge, P.F. James, The factors affecting the thickness of sol-gel derived silica coatings prepared by dipping, J. Non. Cryst. Solids. 86 (1986) 381–393.

[52] S. Dervin, Y. Lang, T. Perova, S.H. Hinder, S.C. Pillai, Graphene oxide reinforced high surface area silica aerogels, J. Non. Cryst. Solids. 465 (2017) 31–38. https://doi.org/10.1016/j.jnoncrysol.2017.03.030.

[53] X. Zhao, Y. Zhu, Y. Wang, Z. Li, Y. Sun, S. Zhao, X. Wu, D. Cao, Hydrophobic, blocky silica-reduced graphene oxide hybrid sponges as highly efficient and recyclable sorbents, Appl. Surf. Sci. 486 (2019) 303–311. https://doi.org/10.1016/j.apsusc.2019.05.017.

[54] C.Q. Hong, J.C. Han, X.H. Zhang, J.C. Du, Novel nanoporous silica aerogel impregnated highly porous ceramics with low thermal conductivity and enhanced mechanical properties, Scr. Mater. 68 (2013) 599–602. https://doi.org/10.1016/j.scriptamat.2012.12.015.

[55] Z.M. Wang, K. Hoshinoo, K. Shishibori, H. Kanoh, K. Ooi, Surfactant-mediated synthesis of a novel nanoporous carbon-silica composite, Chem. Mater. 15 (2003) 2926–2935. https://doi.org/10.1021/cm020965c.

[56] G.P. Fotou, S.E. Pratsinis, N.G. Pinto, Surface area enhancement of silica fibers by sol-gel processes, J. Non. Cryst. Solids. 183 (1995) 135–143. https://doi.org/10.1016/0022-3093(94)00557-5.

[57] C.J. Brinker, R. Sehgal, S.L. Hietala, R. Deshpande, D.M. Smith, D. Loy, C.S. Ashley, Sol-gel strategies for controlled porosity inorganic materials, J. Memb.

Sci. 94 (1994) 85–102. https://doi.org/10.1016/0376-7388(93)E0129-8.

[58] G. Yi, B. Xing, H. Zeng, X. Wang, C. Zhang, J. Cao, L. Chen, One-Step Synthesis of Hierarchical Micro-Mesoporous SiO2/Reduced Graphene Oxide Nanocomposites for Adsorption of Aqueous Cr(VI), J. Nanomater. 2017 (2017). https://doi.org/10.1155/2017/6286549.

[59] P.R. Aravind, P. Mukundan, P. Krishna Pillai, K.G.K. Warrier, Mesoporous silica-alumina aerogels with high thermal pore stability through hybrid sol-gel route followed by subcritical drying, Microporous Mesoporous Mater. 96 (2006) 14–20. https://doi.org/10.1016/j.micromeso.2006.06.014.

[60] M.C. Matos, L.M. Ilharco, R.M. Almeida, The evolution of TEOS to silica gel and glass by vibrational spectroscopy, J. Non. Cryst. Solids. 147–148 (1992) 232–237. https://doi.org/10.1016/S0022-3093(05)80622-2.

[61] D.C.L. Vasconcelos, E.H.M. Nunes, W.L. Vasconcelos, AES and FTIR characterization of sol-gel alumina films, J. Non. Cryst. Solids. 358 (2012) 1374–1379. https://doi.org/10.1016/j.jnoncrysol.2012.03.017.

[62] G. Zu, J. Shen, X. Wei, X. Ni, Z. Zhang, J. Wang, G. Liu, Preparation and characterization of monolithic alumina aerogels, J. Non. Cryst. Solids. 357 (2011) 2903–2906. https://doi.org/10.1016/j.jnoncrysol.2011.03.031.

[63] V. Ţucureanu, A. Matei, A.M. Avram, FTIR Spectroscopy for Carbon Family Study, Crit. Rev. Anal. Chem. 46 (2016) 502–520. https://doi.org/10.1080/10408347.2016.1157013.

[64] A. Bertoluzza, V. Gottardi, M. Guglielmi, C. Fagnano, M.A. Morelli, Raman and Infrarred Spectra on Silica Gel Evolving Toward Glass, J. Non. Cryst. Solids. 48

(1982) 117–128. https://doi.org/10.1016/0022-3093(84)90387-9.

[65] H.D. Ruan, R.L. Frost, J.T. Kloprogge, Comparison of Raman spectra in characterizing gibbsite, bayerite, diaspore and boehmite, J. Raman Spectrosc. 32 (2001) 745–750. https://doi.org/10.1002/jrs.736.

[66] P.P. Nampi, P. Moothetty, F.J. Berry, M. Mortimer, K.G. Warrier, Aluminosilicates with varying alumina-silica ratios: Synthesis via a hybrid sol-gel route and structural characterisation, Dalt. Trans. 39 (2010) 5101–5107. https://doi.org/10.1039/c001219j.

[67] B.E. Yoldas, Effect of ultrastructure on crystallization of mullite, J. Mater. Sci. 27 (1992) 6667–6672. https://doi.org/10.1007/BF01165952.

[68] K. Sinkó, R. Mezei, J. Rohonczy, P. Fratzl, Gel structures containing Al(III), Langmuir. 15 (1999) 6631–6636. https://doi.org/10.1021/la980686x.

[69] M.F. Ashby, Cellular Solids - Scaling of Properties, in: M. Sheffler, P. Colombo (Eds.), Cell. Ceram., 2005: pp. 3–17.

[70] B.E. Yoldas, Preparation of glasses and ceramics from metal-organic compounds, J. Mater. Sci. 12 (1977) 1203–1208. https://doi.org/10.1007/PL00020396.

[71] J.M. Fernández-Navarro, Estructura del vidrio, in: El Vidr., 2003: pp. 64–127.

[72] Y. Zhong, Y. Kong, X. Shen, S. Cui, X. Yi, J. Zhang, Synthesis of a novel porous material comprising carbon/alumina composite aerogels monoliths with high compressive strength, Microporous Mesoporous Mater. 172 (2013) 182–189. https://doi.org/10.1016/j.micromeso.2013.01.021.

[73] S. Akpinar, I.M. Kusoglu, O. Ertugrul, K. Onel, In situ mullite foam fabrication using microwave energy, J. Eur. Ceram. Soc. 32 (2012) 843–848.

https://doi.org/10.1016/j.jeurceramsoc.2011.10.050.

[74] S. Ding, Y.P. Zeng, D. Jiang, Fabrication of mullite ceramics with ultrahigh porosity by gel freeze drying, J. Am. Ceram. Soc. 90 (2007) 2276–2279. https://doi.org/10.1111/j.1551-2916.2007.01696.x.

[75] W.L. Huo, X. Zhang, Z. Hu, Y. Chen, Y. Wang, J. Yang, Silica foams with ultra-large specific surface area structured by hollow mesoporous silica spheres, J. Am. Ceram. Soc. 102 (2019) 955–961. https://doi.org/10.1111/jace.16115.

[76] S. Baharom, S. Ahmad, M.I. Mohd Ramli, The effect of different silica compositions to the properties of silica foam fabricated using slurry method, Mater. Sci. Forum. 888 MSF (2017) 121–125. https://doi.org/10.4028/www.scientific.net/MSF.888.121.

[77] T. Rouxel, Elastic Properties and Short-to Medium-Range Order in Glasses. J. Am. Ceram. Soc., 90 [10] 3019–3039 (2007).

[78] L. Zhang, P. He, K. Song, J. Zhang, B. Zhang, Three - Dimensional Graphene Hybrid SiO 2 Hierarchical dual - network aerogel with low thermal conductivity and high elasticity, (2020) 1–14. https://doi.org/10.3390/coatings10050455.

[79] AZoM, Silica - Fused Silica (Sillicon Dioxide), CiDRA Precis. Serv. Mach. Mater. (2002).

[80] AZoM, Alumina - Aluminium Oxide - Al2O3 - A Refractory Ceramic Oxide, (2001).

[81] Y.Fan, L. Wang, J. Li, S. Sun, F.T. Chen, L. Chen, W.Jiang. Preparation and electrical properties of graphene nanosheet/Al2O3 composites. Carbon 48 (2010) 1743–1749. doi.org/10.1016/j.carbon.2010.01.017

[82] Y.Fan, W. Jiang, A Kawasaki. Highly conductive few-layer graphene/Al_2O_3 nanocomposites with tunable charge carrier type, Adv. Funct. Mat. 22, (2012), 3882-89. https://doi.org/10.1002/adfm.201200632

[83] J. Ru, Y. Fan, W. Zhou, Z. Zhou, T. Wang, R. Liu, J. Yang, X. Lu, J. Wang, C. Ji, L. Wang, W. Jiang, Electrically Conductive and Mechanically Strong Graphene/Mullite Ceramic Composites for High-Performance Electromagnetic Interference Shielding, ACS Appl. Mater. Interfaces. 10 (2018) 39245–39256. https://doi.org/10.1021/acsami.8b12933.

[84] M. Davis, K. Zhang, S. Wang, L.J. Hope-Weeks, Enhanced electrical conductivity in mesoporous 3D indium-tin oxide materials, J. Mater. Chem. 22 (2012) 20163–20165. https://doi.org/10.1039/c2jm34744j.